Geophys. J. Int. (2008) **173,** 593–610 doi: 10.1111/j.1365-246X.2008.03749.x

Lithosphere structure across the Dead Sea Transform as constrained by Rayleigh waves observed during the DESERT experiment

G. Laske,[1] M. Weber[2] and the DESERT Working Group

[1] *Cecil H. and Ida M. Green Institute of Geophysics and Planetary Physics, Scripps Institution of Oceanography, University of California San Diego,* 9500 *Gilman Drive, La Jolla,* CA 92093-0225, *USA. E-mail: glaske@ucsd.edu*

[2] *Sektion* 2.2 *Tiefensondierung, Geoforschungszentrum Potsdam, Telegrafenberg Haus E,* D-14473 *Potsdam, Germany*

Accepted 2008 January 29. Received 2008 January 27; in original form 2007 May 8

SUMMARY

The interdisciplinary Dead Sea Rift Transect (DESERT) project that was conducted in Israel, the Palestine Territories and Jordan has provided a rich palette of data sets to examine the crust and uppermost mantle beneath one of Earth's most prominent fault systems, the Dead Sea Transform (DST). As part of the passive seismic component, thirty broad-band sensors were deployed in 2000 across the DST for roughly one year. During this deployment, we recorded 115 teleseismic earthquakes that are suitable for a fundamental mode Rayleigh wave analysis at intermediate periods (35–150 s). Our initial analysis reveals overall shear velocities that are reduced by up to 4 per cent with respect to reference Earth model PREM. To the west of the DST, we find a seismically relatively fast but thin lid that is about 80 km thick. Towards the east, shallow seismic velocities are low while a deeper low velocity zone is not detected. This contradicts the currently favoured thermomechanical model for the DST that predicts lithospheric thinning through mechanical erosion by an intruding plume from the Red Sea. On the other hand, our current results are somewhat inconclusive regarding asthenosphere velocities east of the DST due to the band limitation of the recording equipment in Jordan.

Key words: Tomography; Surface waves and free oscillations; Transform faults; Dynamics of lithosphere and mantle.

1 INTRODUCTION

The roughly 1000 km long Dead Sea Transform System (DSTS), which includes the Dead Sea rift, provides the essential link between some of the most prominent continental divergent and convergent plate boundaries: the Afro–Arabian Rift System to the south and the Anatolian collision zone and fault system to the north. The transform system is relatively recent (18 Myr). With a present-day slip-rate between Arabia and Africa of 4–5 mm yr^{-1} (Klinger *et al.* 2000a; Wdowinski *et al.* 2004; Mahmoud *et al.* 2005; LeBeon *et al.* 2006; Reilinger *et al.* 2006), the total left-lateral displacement amounts to roughly 105 km (Garfunkel & Ben-Avraham 1996). The DSTS is currently not as seismically active as the southern California part of the San Andreas Fault (about half as many earthquakes make it to the Lamont–Harvard CMT catalogue), but is has nevertheless been the stage for many devastating earthquakes in historical times (Nur & MacAskill 1991; Amiran *et al.* 1994; Klinger *et al.* 2000b; Migowski *et al.* 2004). The last major earthquake, a $M_s = 7.3$ strike-slip event, occurred in 1995 in the Gulf of Aqaba (Hofstetter *et al.* 2003) where the bulk of current seismicity is located. More recently, a $M_L = 5.3$ earthquake beneath the northern Dead Sea on 2004 February 11 damaged structures in Jerusalem, Tel Aviv and Nablus 50 km away, and five $M_L = 4.0$ or larger events have occurred in the greater Dead Sea region since then (Geophysical Institute of Israel online event catalogue). Such events and the frequent microseismic activity (e.g. van Eck & Hofstetter 1990; Aldersons *et al.* 2003; Salamon *et al.* 2003) are but reminders of the imminent seismic hazard in the region. The DSTS also hosts the Dead Sea, the deepest depression, and the Dead Sea basin, the largest pull-apart basin known on Earth. The Dead Sea basin is almost 150 km long, about 10 km wide and extends from the southern Jordan valley near Jericho through the central Arava (or Araba) valley north of Elat. The Dead Sea Transform (DST) is governed by a relatively simple stress field which puts it in marked contrast to other major fault systems (e.g. the North Anatolian Fault or the San Andreas Fault Systems). This simplicity provides the opportunity for a 'natural laboratory' to study active transform faults, a key structural element of plate tectonics. There have been a few active source experiments in the past to study crustal structure on both sides of the DST (e.g. Makris *et al.* 1983; Mechie & El-Isa 1988). But despite the central role of the DSTS as a 'world geological site', no geophysical transect has ever crossed it so that many details of the crustal and upper-mantle structure and its role in the dynamics of this region are still unknown.

An international team with colleagues from Germany, Israel, the Palestine Territories and Jordan therefore joined forces to conduct an interdisciplinary, multiscale study of the Dead Sea Rift (Abu-Ayyash *et al.* 2000; DESERT Group 2004). The DEad SEa Rift Transect (DESERT) was launched in 2000 February and addresses such fundamental questions as 'How do shear zones work?' and 'What controls them?' The first DESERT field campaign consisted of several

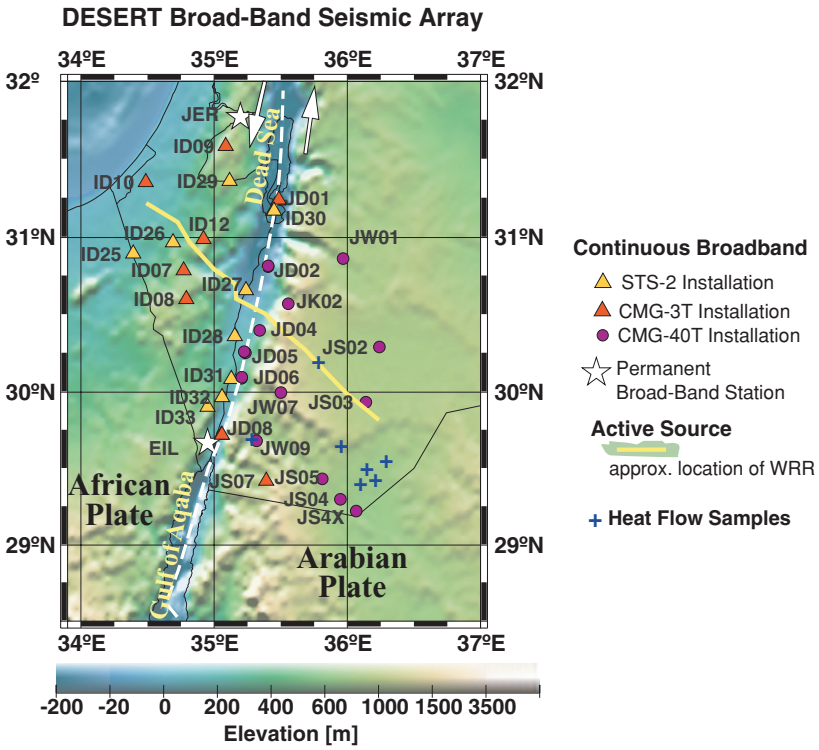

Figure 1. Array configuration of the passive seismic components of the DESERT experiment. The small-aperture (several km) controlled source array as well as an MT array were located along the wide-angle refraction and reflection (WRR) line across the Dead Sea Basin. Stars mark permanent broad-band stations the data for which are easily accessible through Data Management Centers. The present-day relative plate motion (white arrows) is about 5 mm yr^{-1}. Blue crosses mark locations of measured conductive surface heat flow (Galanis *et al.* 1986; Förster *et al.* 2007). The white dashed line approximately marks the Dead Sea Transform boundary. The Dead Sea Rift is characterized by low elevations between the Dead Sea and the Gulf of Aqaba.

active seismic, magnetotelluric and passive seismic projects where the latter lasted until 2001 June (Fig. 1). DESERT also includes electromagnetic, gravity, geodynamic, petrological, geothermic and geotechnical studies.

The centrepiece of the active seismic component of DESERT is a 300-km-long profile across the Dead Sea Basin (Fig. 1) that includes a wide-angle reflection/refraction study (WRR), a near-vertical reflection study (NVR) and a high-frequency controlled source array. Results from the active seismic studies have recently started to appear in the literature (Haberland *et al.* 2003; DESERT Group 2004; Maercklin *et al.* 2004; Mechie *et al.* 2005; Kesten *et al.* 2008). To summarize some of the results, the damage zone within the fault is only a few tens of metres wide and therefore much narrower than that of the San Andreas Fault. The Moho depth along the WRR line gradually increases from 28 to 38 km but, perhaps surprisingly, no significant Moho-updoming is observed under the Dead Sea rift. This observation taken by itself suggests that the mantle has played a minor role in the extension process associated with the rift itself (DESERT Group 2004). This also appears to be in concordance with the 'normal' surface heat flow of 45–60 mW m^{-2} on the uplifted Arabian Plate to the east of the DST (Eckstein 1979; Förster *et al.* 2007).

DESERT also has a passive seismic component carried by a 30-instrument broad-band array (Güralp CMG-3T and CMG-40T as well as Wielandt-Streckeisen STS-2 sensors) and a 30-instrument short-period array (Mark L4-3D sensors), all instruments recording continuously at 50 Hz. The driving force for setting up the passive seismic array was to augment body wave tomographic data sets (Koulakov & Sobolev 2006; Koulakov *et al.* 2006), and to analyse receiver functions (Mohsen *et al.* 2005, 2006) and shear wave splitting (Bock *et al.* 2001; Rümpker *et al.* 2003; Ryberg *et al.* 2005). Detailed thermomechanical modelling that has been carried out as part of DESERT indicates that the mantle must be involved in the deformation process in order to explain the marked offset in topography (more than 1 km) across the DSTS (Sobolev *et al.* 2005). In their favoured scenario the lithosphere of the Arabian Plate underwent thinning through either thermal erosion or delamination, while the lithosphere west of the DST remains unaffected. This is consistent with the results from the receiver function study of Mohsen *et al.* (2006) who detect the top of a low-velocity zone east of the DST, which is assumed to be the lithosphere-asthenosphere boundary (LAB), to deepen northward from 67 to 80 km depth. Sobolev's scenario is also broadly consistent with the results of large-scale surface wave studies by Debayle *et al.* (2001) and Maggi & Priestley (2005) who find anomalously low velocities beneath the Arabian Plate at about 100 km depth.

Though initially not a target area, the data analysis appears to reveal that the seismic structure of the deeper upper mantle, that eludes most of the initially planned seismic components of DESERT, holds the clues to understanding the geodynamical state of the DSTS. A Backus–Gilbert analysis (Backus & Gilbert 1968) reveals that seismic surface waves between 15 and 100 s provide useful complementary information on local crustal and upper-mantle structure down to at least 250 km (Fig. 2). Reliable broad-band instrumentation actually provides high-quality data to much longer periods, so our estimates are rather conservative. The original DESERT proposal included no plans to analyse surface waves but it may now be a key study tool. A regional analysis of surface wave dispersion is also

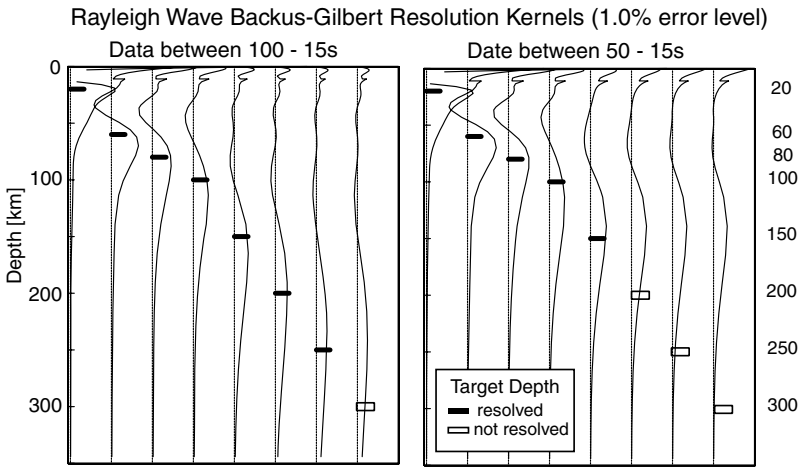

Figure 2. Results of a Backus–Gilbert resolution analysis, for two sets of given input dispersion data (the two period band 100–15 s and 50–15 s). The vertical functions show over what range a δ-function like structure will be spread, assuming a 1 per cent error in our data. Horizontal bars mark the 'target depth', the depth at which the δ-function was placed. Solid bars indicate that a target depth is resolved (i.e. structure recovered at the right depth), while open bars mark target depths that are not resolved. Dispersion data at periods longer than 50 s period are clearly needed to resolve structure below 150 km. Assuming that we gather no useful data beyond 100 s implies that our data set will not resolve structure at 300 km depth and beyond.

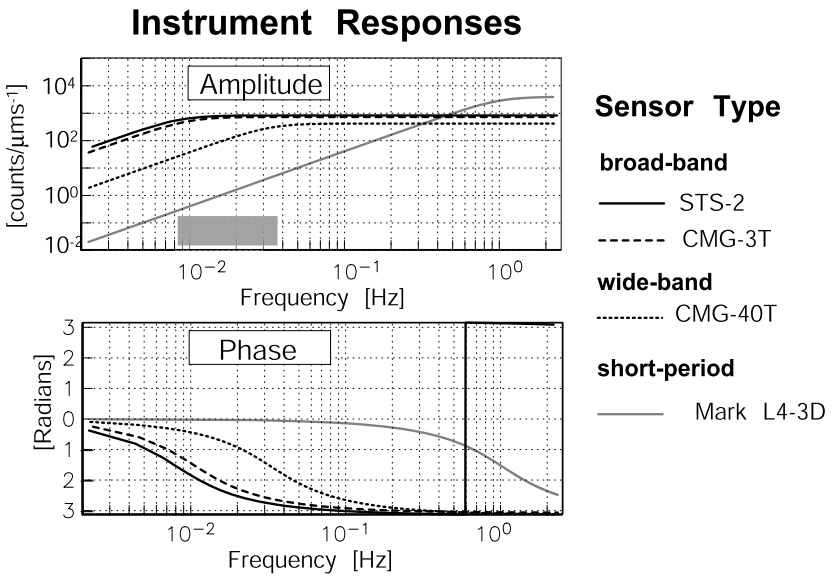

Figure 3. Ground velocity responses for a variety of instruments discussed in this paper. STS-2 and CMG-3T equipment are true broad-band instruments, while the CMG-40T has considerably less bandwidth. Also shown is the LP-end of the response of short-period Mark L4-3D equipment. The grey bar marks the frequency range of the surface waves analysed here.

one of the few tools that provide absolute seismic velocities. In this paper, we present our initial teleseismic Rayleigh wave analysis for periods between 35 and 150 s. Our model exhibits a thin, seismically fast mantle lid west of the DST that is underlain by a pronounced low-velocity zone (the asthenosphere), as predicted by the geodynamic model. On the eastern side, however, shallow seismic mantle velocities are much lower and a low-velocity zone beneath is not imaged everywhere. This suggests that the root of the Arabian Shield away from the DST may still be intact.

To the east of the DST, our current model has greater uncertainties than we desire. Due to logistical reasons, the area east of the DST was occupied mainly by wide-band CMG-40T sensors (see Fig. 1). This strategy was irrelevant for the initially planned body wave experiments but greatly hampers a surface wave study, as the CMG-40T cannot record long-period signals with high fidelity. Fig. 3 shows that the low-frequency roll-off in the velocity response for the CMG-40T is at periods around 33 s, while the roll-off at true broad-band sensors is around 100 s. The nominal corner frequencies of the CMG-40T on one hand and the CMG-3T and STS-2 on the other are 40 and 120 s (see e.g. at the web site of the PASSCAL program, http://www.passcal.nmt.edu/instrumentation/Sensor/sensor_info.html). Taking this information at face value, we could probably expect to measure dispersion to 50 s but not much more, at a significant loss of resolution below 150 km (Fig. 2). We were initially skeptical that an analyse of CMG-40T records can be done for our purposes, as some tests in the field and on the pier in a vault appear to have been quite discouraging. The sensor is reported to become quite noisy at periods much longer than 15 s (Frank Vernon 2002, and Jim Fowler, 2003, personal communication). On the other hand, the signal-to-noise ratio in individual

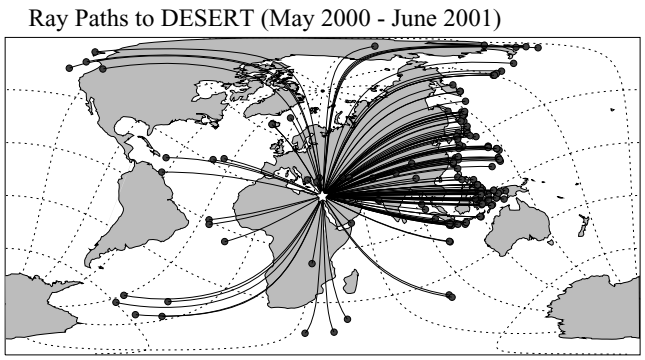

Figure 4. Events suitable for a teleseismic surface wave study at the DESERT array. Selection criteria are: epicentral distance less than 105°; source depth less than 110 km; scalar seismic moment greater than 5×10^{17} Nm.

seismograms depends strongly on ambient noise and installation conditions, and source parameters such as earthquake magnitude. However, our own experience in low-frequency studies has taught us that reliable measurements are possible on broad-band sensors much beyond the low-frequency roll-off. The fact that dispersion has been measured on Mark L4-3D 1 Hz sensors to periods up to 50 s (Forsyth *et al.* 1998), though this was on the ocean floor, ultimately encouraged us to attempt the study presented here. During the DESERT deployment, we collected numerous seismograms of almost spectacularly high quality that appears to disprove the rather pessimistic view of some of us. Nevertheless, we most likely would have chosen a different deployment plan had a surface wave component been part of the initial proposal. In this regard, the analysis presented here summarizes the 'lessons we learnt'.

2 DESCRIPTION OF THE FIELD PROGRAM

The project concentrates on the area around the Arava Valley at the southern end of the DST. DESERT is the first experiment of its kind that is conducted concurrently on both sides of the DST. The passive seismic component of the DESERT program began with the deployment of CMG-3T and CMG-40T sensors in 2000 May, while STS-2 sensors followed in 2000 November to augment the deployment west of the DST and south along the Arava Valley (Fig. 1). Except for station JS07, all sites east of the DST were equipped with CMG-40Ts. The majority of sites in Jordan were collocated with stations of a permanent seismic network, while about half the installations in Israel were located in bunkers. All stations were recovered in 2001 June.

2.1 Data collection, processing and availability

For the period between 2000 May and 2001 June, we can identify numerous shallow teleseismic earthquakes that are suitable for this study (Fig. 4). Our database includes 115 shallow events with a scalar seismic moment of $M_0 = 5 \times 10^{17}$ Nm or greater which corresponds roughly to surface wave magnitudes $M_S > 4.7$. The azimuthal coverage is very good though events occurring along the Western Pacific Rim dominate the database.

The original data are sampled at 50 Hz which is impractical for a long-periods surface wave analysis. We therefore low-pass filter the data using a steep convolution filter and decimate the data to 1 Hz. In unprocessed records, data around 20 s usually dominate the spectrum of the wave trains. At teleseismic distances, such data have

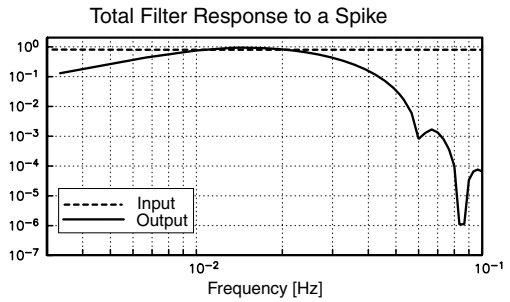

Figure 5. Data filtering response (solid) to a synthetic spike (dashed). A combination of demeaning and two low-pass filters is applied prior to removal of the instrument response, and a high-pass and a low-pass filter afterward.

undergone significant multipathing before arriving at the recording array, which hampers a straight-forward analysis. We suppress the dominance of these data using another, less steep low-pass filter before removing the instrument response. To 'pre-whiten' the data, we finally apply a combination of high- and low-pass filters. The response of the complete set of four filter cascades is shown in Fig. 5.

Fig. 6 gives a rough idea of the data return. We were not involved in the routine data quality control (QC) and the figure shows only the recovery for earthquakes used in this study. Nevertheless, it provides important insight into data restrictions imposed on the surface wave study described in this paper. Most stations recorded continuously during their deployment and provided useful seismic data but some sites performed less well. For example, site JS05 has a several-months long period during the first half of the deployment in which it did not return any useful long-period data. Site JS04 was relocated in 2000 November, after recording only few events in May and September/October and losing the GPS signal. Station ID09, which was located in a private backyard in Hebron, stopped recording in July. One or both horizontal components failed temporarily at stations ID08, ID10, ID12, ID26 and ID30. The failure at ID10 is particularly disappointing because its near-shore location at the northwestern end of the array could have provided valuable reference data outside of the DST area. For unknown reasons, ID10 was noisy between August and November. New Year 2001, both its horizontal components failed. Starting near the beginning of 2001 March, the horizontal components were back but all 3 components exhibit a suspicious, time-dependent time offset with respect to other stations. The offset is not the same for different phases in a seismogram, that is, the offsets grow between the *P*, *S* and surface wave packets. A simple clock error therefore has to be excluded as possible cause. The time-dependent offset is likely explained by a change in sampling rate (Jim Mechie, personal communication) and was likely caused when incompatible electronic components where combined in the data loggers (Karl-Heinz Jäckel, personal communication). This problem was detected after the DESERT experiment was already completed. A similar though much more limited problem occurs at station ID33. The surface wave dispersion measured for such records is physically implausible and has to be discarded because we have no straightforward strategy to correct for the technical problem. Fig. 6 also provides information on the quality of individual surface wave packets. This is discussed in the next section.

2.2 Data examples and data quality

Fig. 7 shows a record section of the 2000 June 18 earthquake in the South Indian Ocean when only CMG-3T and CMG-40T sensors

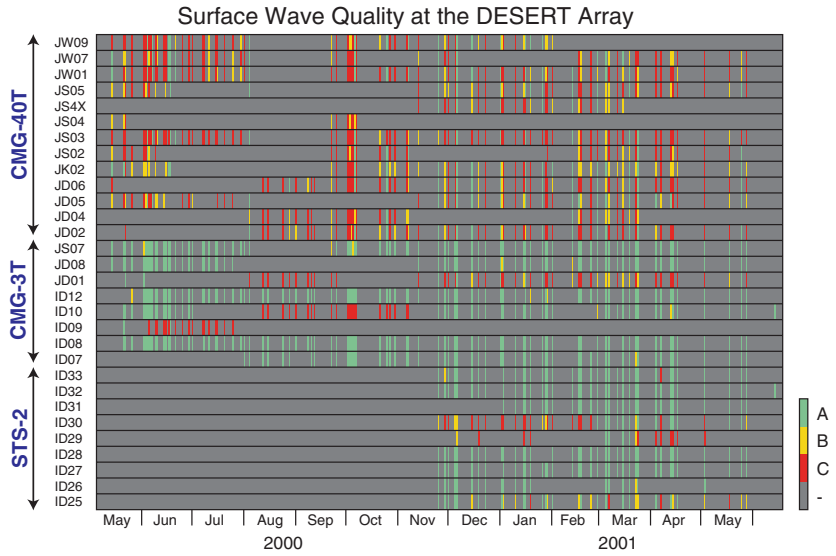

Figure 6. Catalogue and quality of the surface wave records at each DESERT station. Shown are records with high signal-to-noise ratio (grade A; green bar), with some noise (grade B; yellow bar), and with a signal-to-noise ratio close to 1 (grade C; red bar). The absence of a colour bar at a station, for a certain earthquake, indicates that no useful long-period data are available (grade D or the station was not operational). The overall surface wave quality at the CMG-40Ts is clearly diminished but some earthquakes produced grade A seismograms for these sensors.

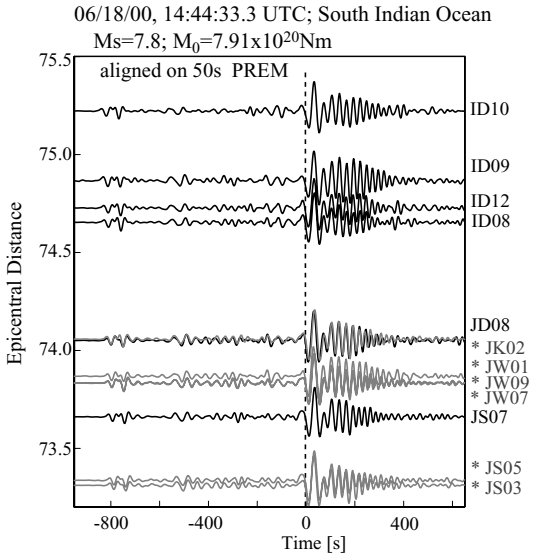

Figure 7. Data example of ground acceleration for the 2000 June 18 South Indian Ocean earthquake (grey: CMG-40T; black: CMG-3T). The signals are aligned with PREM predicted traveltimes (Dziewonski & Anderson 1981) for 50s Rayleigh waves. The data were bandpass filtered using the series of convolution filters described in the text.

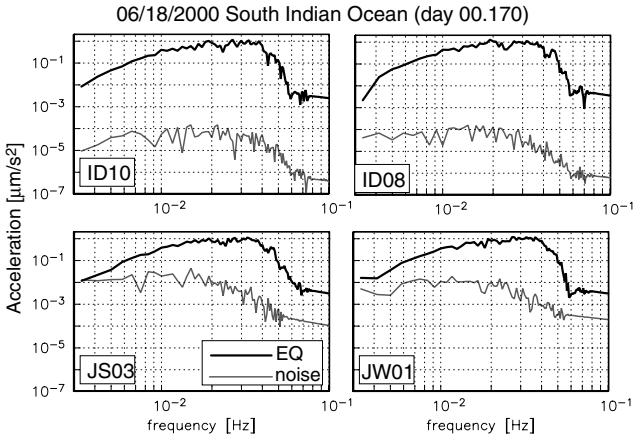

Figure 8. Spectra of noise (grey lines) and surface wave signals (black lines) for some of the records of the 2000 June 18 South Indian Ocean earthquake from Fig. 7. Stations ID10 and ID08 had a broad-band sensor (CMG-3T), while JS03 and JW01 had a wide-band sensor (CMG-40T). The underlying time-series are 20 min long, a boxcar window is applied and the spectra are normalized by the record length. Note that the ground accelerations shown here are not true accelerations as the spectra are affected by our preconditioning using the filter from Fig. 5.

were operating (see Fig. 6). Visual inspection of the seismograms suggests that the CMG-40Ts provided excellent data for this earthquake that was roughly 74° away from the DESERT array. This earthquake was the second largest event during the deployment so the good data quality is perhaps not surprising. The acceleration spectra in Fig. 8 give insight down to which frequency we can expect to obtain reliable dispersion data. On the two broad-band sensors (CMG-3T at ID10, ID08), the noise floor recorded prior to the event lies about 10^3–10^4 decades below the seismic signal, in the entire band between 3 and 60 mHz (roughly 300 to 17 s). On the two wide-band sensors (CMG-40T at JS03, JW01), the noise floor is much higher and therefore closer to the seismic signal. In fact, the noise approaches the signal at very low frequencies, so the SNR approaches 1. At 10 mHz (100 s), the SNR is at least 10 so we are confident that dispersion analysis is possible.

Fig. 9 shows records for an earthquake that occurred three days later in Iceland. Its scalar seismic moment, M_0, was roughly 150 times smaller than that of the south Indian Ocean event. The surface waves clearly stand out from the background noise though earlier arriving long-period body wave phases (e.g. arrivals near the −400 s mark) are now harder to discern on the CMG-40T records. A total of 33 earthquakes in our database have scalar seismic moments of $M_0 = 4 \times 10^{18}$ Nm or larger so the example shown here is representative of an earthquake delivering good-quality records. The spectra

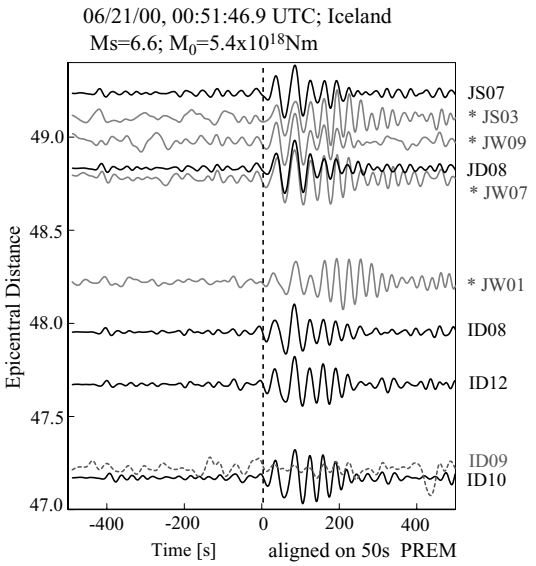

Figure 9. Data example of ground acceleration for the 2000 June 21 Iceland earthquake. For details see Fig. 7. Due to high noise levels, station ID09 returned no useful signal for this earthquake. Stations JK02 and JS05 that recorded the June 18 South Indian Ocean earthquake three days before produced no data for this event nor through at least 2000 July (see Fig. 6).

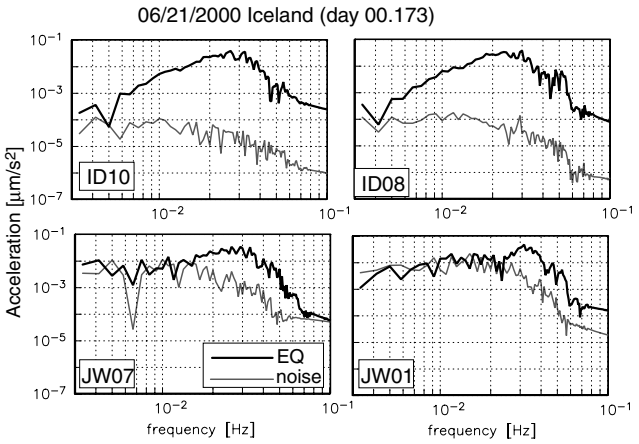

Figure 10. Spectra of noise and surface wave signals for some of the records of the 2000 June 21 Iceland earthquake from Fig. 9. For details see Fig. 8.

in Fig. 10 indicate that a surface wave analysis should be possible for frequencies down to 5 mHz ($T = 200$ s), at the broad-band sensors such as at stations ID10 and ID08. Due to the higher noise levels at the wide-band sensors, the frequency range there is now rather limited, for example, to frequencies above 20 mHz ($T = 50$ s) at JW01 and above 13 mHz ($T \simeq 75$ s) at JW07. We want to stress however, that the signal level is sufficient to reliably analyse surface waves much beyond the anticipated 15 s or so.

A severe distortion of the record prior to the arrival of the earthquake signal at JS03 hampers a reliable noise analysis but inspection of Fig. 9 suggests that the noise levels may be somewhat higher, as is the case for JW09. In a somewhat subjective but systematic assessment of waveform quality, we inspect all seismograms individually and assign grades A–D. We assign an A, if the surface wave signal stands out clearly above the background noise. If the noise level is significant, obscuring prior body wave arrivals, we assign a B. Grade C is assigned to records for which a surface wave train is difficult to discern and grade D is assigned when no obvious surface wave train can be observed, for the frequency range used here. For the Iceland event, the record at ID09 is a D while the records at JS03 and JW09 are marginally B. Inspecting Fig. 6 we find a clear difference in performance between broad- and wide-band sensors. While most stations equipped with a CMG-3T or an STS-2 sensor reliably return A quality waveforms, stations with CMG-40T are much less likely to do so. The broad-band sensors at the DESERT rarely give grade C records unless there is an obvious installation problem (e.g. stations ID09, ID10 and JD01 which was located in a chamber of a permanent seismic station). Fig. 11 reveals that poor grades are typically assigned to wide-band records of smaller earthquakes, while broad-band records are still grade A. A dependence on epicentral distance is also apparent though we have not many events at distances shorter than 60° to assess this quantitatively. There are significant performance differences among wide-band stations but a good station can provide many grade A and B records. From the quality assessment shown here, it is quite obvious however that the installation of a wide-band sensor is not ideal for a long-period surface wave analysis and limits the number high-quality dispersion data significantly.

3 MEASURING DISPERSION—THE TRIANGLE METHOD

For each event, we measure the frequency-dependent relative phase between two seismograms, or differential dispersion, using the transfer function approach that we apply in our global studies (Laske & Masters 1996). The only difference is that here we measure the phase at each station with respect to other stations in the array instead of measuring the phase with respect to an individual source–receiver 1-D synthetic (Laske *et al.* 1999, 2007). As reference seismograms, we chose only those of broad-band stations, due to their better SNR. Our final database includes 9290 sets of differential dispersion which provide the input data for the triangle method for which the phase at each station is reconstructed from the differential dispersion data using the same reference station. The great similarity of waveforms in a regional study leads to differential dispersion that is significantly less than if compared to 1-D synthetics. In our DESERT phase data set the rms amounts to only 0.4 per cent. In our study at the temporary Saudi Seismic Network where we used global 1-D synthetics as reference, the rms was 0.85 per cent (Laske & Cotte 2000). The mean measurement error is also smaller, with 0.02 per cent for the DESERT data set while it was 0.07 per cent for the Saudi data set.

Regional surface wave studies using teleseismic events often resort to the two-station method where dispersion is analysed for earthquakes that lie on a two-station great circle (e.g. Woods & Okal 1996; Meier *et al.* 2004). While we have applied such a technique successfully in the Pacific Ocean (Laske *et al.* 1999, 2007) we find in those studies that wave packets traversing continental areas may undergo significant lateral refraction. As mentioned above, our data set is dominated by earthquakes along the western Pacific Rim. Surface waves emerging from the area north of Japan traverse the Eurasian Continent north of China and the Tibetan Plateau and graze one of the most pronounced large-scale low-velocity anomalies on the globe (e.g. Ekström *et al.* 1997). Surface waves travelling along this corridor experience particularly strong lateral refraction and even multipathing may be significant (e.g. Laske & Cotte 2001). Our pre-analysis assessment of the data set includes inspection of the complete three-component records and the measurement of arrival angles (see Appendix A). From the particle motion analysis at the DESERT array we find that surface waves can arrive at a station

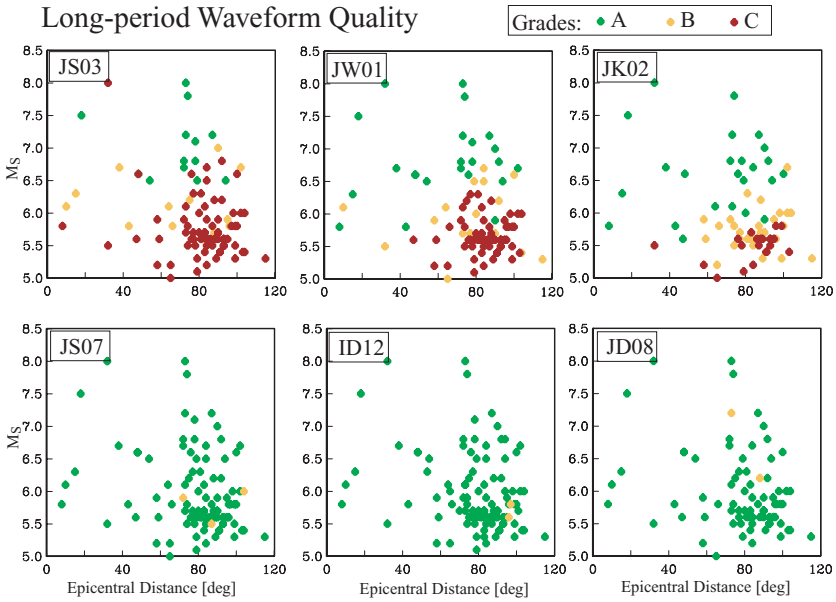

Figure 11. Long-period waveform quality at six stations, as function of epicentral distance and surface wave magnitude M_S. Grade 'D' seismograms are omitted from this figure. For details see Fig. 6.

well beyond 10° away from the expected great circle direction. This effectively shortens the travel path between two stations and, if not accounted for properly, biases estimated phase velocities high by 1.5 per cent which is a significant fraction of the signal we expect from local heterogeneity across the DST. We therefore choose not to use the two-station approach.

Instead, we use an array processing technique that allows us to fit approaching wave fronts to the phases of several stations simultaneously (e.g. Alsina & Snieder 1993; Stange & Friederich 1993). In our most basic approach, we fit spherical wave fronts to the phase of three stations simultaneously. We refer to this approach as the triangle method. Wave propagation within the triangle is assumed to be at a constant velocity where the distortion of the wave front depends only on geometrical spreading (see Fig. 12). Off-great circle propagation between the source and the triangle is accounted for by allowing an arrival angle as second free parameter in a grid search to minimize the prediction error for the phase triplet, as function of frequency. We perform this search by moving the source in increments of a fraction of a degree in each direction. In a similar study off Hawaii, we had experimented with fitting plane waves to station triangles (Laske *et al.* 2007) but we found that such a strategy gives higher data misfits and less consistent dispersion curves for different events. We suspect that the plane wave approach oversimplifies the actual evolution of the wave fronts across the triangle which depends on the epicentral distance and the orientation of the triangle relative to the source. In a plane geometry, the back azimuth to the source is the same for all three stations, which is not the case on a spherical earth. Fig. 12 shows plane waves reconstructed from the normals to the source–receiver rays for the South Indian Ocean earthquake. If we propagate these plane waves from early stations and those at the periphery of the array (e.g. JS07) to a later station (e.g. ID10), we observe a mismatch between the propagated wave fronts and the actual normal to the ray at this later station. This mismatch can be significant. For example, at an epicentral distance of 47–48°, the Iceland event of Fig. 9 has backazimuths of 330.4°, 330.3° and 331.8° at Stations ID10, ID30 and JS07. Assuming an average of 331° in a plane geometry misrepresents the propagating wave front and biases the related average phase velocity between ID10 and ID30 low by 1.6 per cent, which is obviously unacceptable. Wielandt (1993) and Friederich *et al.* (1994) showed that the wave field of teleseismic earthquakes observed at stations in Central Europe may be quite complicated and that rather complex wave fields have to be included as additional unknowns in the modelling of the phase and amplitude at each station. Such a problem almost certainly has non-unique solutions. The station triangles at the DESERT array are so small that our assumption of a uniform wave field may be acceptable. This idea is supported by the fact that we use only events for which the waveforms are extremely coherent across the array. We should also point out that analyses for larger triangles may have to take source effects into account. Due to the different deployment times of the equipment, the choice of suitable triangles is greatly dictated by the data availability. For this study, we analyse 22 triangles (Table 1).

3.1 Measurement uncertainties

To measure the phase in a seismogram relative to a reference seismogram, we apply a multitaper technique to determine the complex transfer function between the two (Park *et al.* 1987). Using a jackknife procedure, this allows us to obtain formal error bars for each phase measurement (Laske & Masters 1996). Raw phase errors of individual measurements depend on frequency and can be as small as 0.2 radians but are typically around 0.4 radians. At periods longer than 100 s, this may be too large to measure dispersion precisely enough to resolve subtle velocity anomalies. For example, at $T =$ 100 s and a travel distance of 100 km within a station triangle, a 10 per cent phase velocity anomaly gives rise a phase difference of only 0.15 radians. A single measurement is therefore not sufficient to resolve long-period dispersion adequately, especially when a typically noisier CMG-40T record is involved. However, as described above, we measure the phase at a station relative to several reference seismograms from other stations which significantly decreases the phase error for a given earthquake and station.

To convey a rough idea of data accuracy in the triangle method, Fig. 12 shows the dispersion curves of 3 triangles that share an

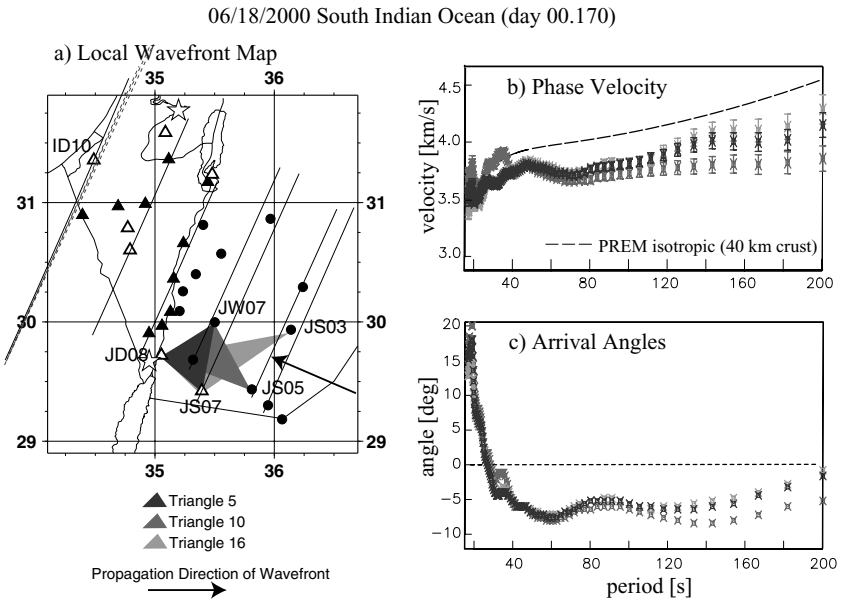

Figure 12. Local wave fronts, phase velocities and arrival angles for the 2000 June 18 South Indian Ocean event obtained with the triangle technique, for three triangles in the southeastern corner of the DESERT array. (a) Location of the triangles and local wave fronts for some stations (normals to the source–receiver rays). The propagation of these local wave fronts across the array as plane waves causes a mismatch near the end of the arrays (dashed lines at station ID10; the mismatch is slightly exaggerated for display). (b) Measured dispersion curves. The triangles cover similar areas so the dispersion curves should be very similar. Phase velocities are significantly lower than those predicted with PREM (Dziewonski & Anderson 1981), assuming a 40 km thick crust (dashed line). (c) Arrival angles (deviation from the event backazimuth) can reach 10° which indicates that lateral refraction by heterogeneous structure between the source and the DESERT array diverted the wave packets away from the source–receiver great circle. At periods much shorter than 35 s, arrival angles increase and phase velocities become oscillatory and inconsistent. This is possibly a consequence of multipathing between the source and the DESERT array, and related distortion of the wave front. The triangle method may not work for these cases.

Table 1. Station triangles analysed in this study.

Triangle	Stations	Area (km^2)	Centre location	No. of earthquakes	No. of GMG-40Ts
1	ID10 ID08 ID30	3513	34.91E 31.04N	2	0
2	ID08 ID10 JW01	5130	35.08E 30.94N	16	1
3	ID08 ID25 ID30	2220	34.88E 30.89N	7	0
4	ID08 ID27 ID32	1595	35.03E 30.41N	43	0
5	JD08 JS07 JW07	1222	35.32E 29.71N	19	1
6	JD08 ID28 JW07	1394	35.24E 30.03N	11	1
7	ID28 JS02 JS07	5359	35.60E 30.03N	5	1
8	JS07 JW07 JS03	1997	35.68E 29.78N	14	2
9	ID27 ID31 JS02	3283	35.54E 30.35N	5	1
10	JD08 JW07 JS05	1815	35.46E 29.72N	10	2
11	ID27 JW01 JS02	2514	35.82E 30.61N	5	2
12	JD08 ID28 JS03	3612	35.45E 30.01N	11	1
13	JD08 ID28 JS02	3747	35.48E 30.13N	5	1
14	ID25 ID30 ID32	6152	34.97E 30.68N	7	0
15	JD08 ID30 JS03	7989	35.55E 30.28N	4	1
16	JS07 JD08 JS03	2134	35.53E 29.69N	15	1
17	JS05 JS03 ID32	2956	35.67E 29.78N	8	2
18	JS4X JD08 JS03	4293	35.75E 29.61N	6	2
19	ID25 ID29 ID12	945	34.81E 31.08N	5	0
20	ID26 ID27 ID30	1824	35.12E 30.93N	5	0
21	ID25 ID29 ID27	2999	34.92E 30.97N	5	0
22	ID30 ID27 JW01	1757	35.55E 30.90N	4	1

area in southern Jordan. The dispersion curves are quite similar at periods between 35 and 125 s (28.5 and 8 mHz) which gives us confidence in the long-period data. However, the dispersion curves divert at periods much longer than that, which is most likely due to the limitations of our technique (triangles too small, phase errors too large) rather than deep-seated lateral heterogeneity. We also refrain from interpreting dispersion at periods much shorter than 35 s. Such data could potentially reveal crustal shear velocity structure but the scatter in the data suggest that multipathing effects between the teleseismic source and the array distort the waveforms enough to hamper an analysis using the spherical wave front approach in the triangle technique. In the wave front fitting, some of this multipathing

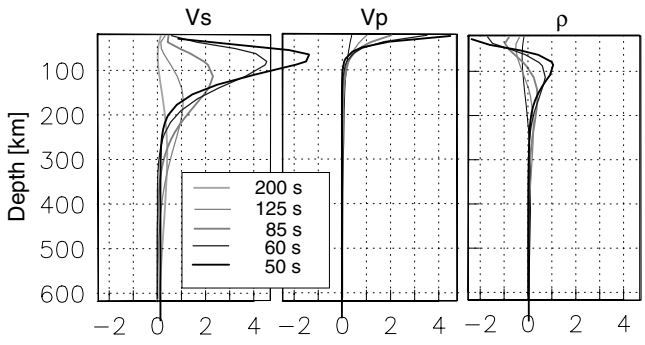

Figure 13. Rayleigh wave sensitivity kernels for isotropic structure at depth. Rayleigh waves depend on V_S, shallow V_P as well as density, ρ, but sensitivity to V_S dominates. The model used to calculate the kernels is spherical reference model 1066A (Gilbert & Dziewonski 1975).

may actually be taken up by the arrival angle which, in turn, has a smoothing effect on the phase velocity curve.

4 INVERSION FOR STRUCTURE AT DEPTH

We retrieve structure at depth in two steps. First we determine average depth-profiles for each triangle. All profiles are then combined to display 3-D structure.

Surface waves are sensitive to V_S, V_P and density, ρ but the most dominant and best resolved parameter is V_S (Fig. 13). In order to limit the number of model parameters for a well conditioned inverse problem, tomographers often ignore sensitivity to V_P and ρ. Such a strategy could lead to biased models where shallow V_P structure can be mapped into deeper V_S structure. We prefer to scale the kernels for V_P and ρ and include them in a single kernel for V_S, using the following scaling:

$$\begin{aligned} \tilde{A} \cdot \delta\alpha &= (1/1.7)\tilde{B} \cdot \delta\beta \\ \tilde{R} \cdot \delta\rho &= (1/2.5)\tilde{B} \cdot \delta\beta. \end{aligned} \tag{1}$$

The scaling factors were determined in both theoretical and experimental studies (e.g. Anderson *et al.* 1968; Anderson & Isaak 1995), for high temperatures and low pressures such as we find in the upper mantle. They are applicable as long as strong compositional changes or large amounts of melt (i.e. >10 per cent) or attenuation do not play a significant role (e.g. Karato 1993). As starting model, we use a modified version of isotropic PREM (Dziewonski & Anderson 1981) in which the negative velocity gradient above 220 km and the discontinuity at 220 km are removed. The crustal thickness is fixed to 33 km. This thickness was chosen from an average of data that constrain the global crustal model CRUST2.0 (Bassin *et al.* 2000). It is also consistent as an average along the WRR profile for which the Moho was found at 26 km depth at the northwestern end and at nearly 40 km at the southeastern end (DESERT Group 2004; Mechie *et al.* 2005). To avoid a strong trade-off between errors in Moho depth and shallow mantle velocity, we include a crustal layer in our model. Detailed modelling attempts for triangle #3 also revealed that velocities in the mantle remain largely independent of a moderate change in the Moho of the starting model, if we do not include dispersion at frequencies above 28.5 mHz (periods shorter than 35 s) in the inversions. In the mantle, our model has 14 layers whose thickness increases with depth to account for the increasing resolution length: 13 km near the top to 20 km near the bottom, except for the last layer which is 30 km thick. The bottom of the lowermost layer is 287 km. At this depth, sensitivity of our data is expected to be weak but the inclusion of a deep layer avoids erroneous imaging of such a deep structure into shallower layers.

We seek smooth variations to the starting model in a linear, direct matrix inversion that fit our data to within an acceptable misfit, χ^2/N, where $\chi = x_d - x_t$, x_d is the datum, x_t the prediction and N the number of data. Formally, we seek to minimize the weighted sum of data prediction error, χ^2, and model smoothness, $\partial\mathbf{m}$

$$\chi^2 + \mu \left| \mathbf{m}^T \partial^T \partial \mathbf{m} \right|, \tag{2}$$

where $\mathbf{m}$ is the model vector and μ the smoothing or regularization parameter (see Laske & Masters 1996; Laske *et al.* 2007, for details) . The two terms can be plotted against each other in a trade-off curve, as function of the regularization parameter μ. The exact shape of the trade-off curve depends on the data errors as well as the composition of the data set but the resulting optimal models are similar to the ones shown in the following. Usually, the trade-off curve is L-shaped and a model is often chosen near the bend where both the misfit of the data and model roughness do not change much when μ is varied. In our inversions, such models are somewhat oscillatory and we choose smoother models. Model errors can be obtained from the data errors through a formal singular value decomposition or by Monte Carlo forward modelling. The error bounds shown here represent the range of acceptable models along the trade-off curve. The final models have misfits, χ^2/N, between 1.0 and 1.5 so are slightly inconsistent with the data.

5 VELOCITY MODELS ACROSS THE DESERT ARRAY

Taking the approach just described, we determine average dispersion curves for the 22 triangles of Table 1. We notice consistent significant changes between triangles of different areas. In this section, we show examples for the three most distinct groups. For a group west of the DST (Fig. 14; Group 1), we observe phase velocities at short periods that reach PREM values but lower velocities at longer periods. This must result from relatively shallow mantle structure with high velocities but lower velocities further down. The inversion for shear-velocity profiles gives models with relatively high velocities in the lithosphere, down to at least 75 km. With values reaching 4.43 km s^{-1}, these are the highest found across the DESERT array. Down to depths of 60 km, they nearly agree with PREM but then reduce to values significantly lower than PREM. At 80 km, the velocities we observe are 3.6 per cent lower than in PREM. This discrepancy remains to at least 200 km depth where velocities approach or fall below 4.25 km s^{-1} (4 per cent lower than in PREM). To summarize, we find a relatively thin lithosphere of no more than 80 km thickness and an anomalously slow asthenosphere, especially towards the south. Since our data do not extend much beyond 120 s, they cannot constrain the bottom of the asthenosphere. At greater depths, higher velocities are found near the north though this trend may not be significant (see discussion on errors). At periods between 60 and 80 s, the predictions appear slightly inconsistent with the observations. The reason for this is most likely because error bars are smaller at periods between 35 and 50 s so these data, that best constrain the topmost part of the lithosphere, have more weight in the inversion. We currently cannot find a realistically smooth model that fits all data equally well.

A second category of dispersion curves is that of Group 2 (Fig. 15), for which we observe lower phase velocities than for Group 1 triangles, in the entire period range. This points towards

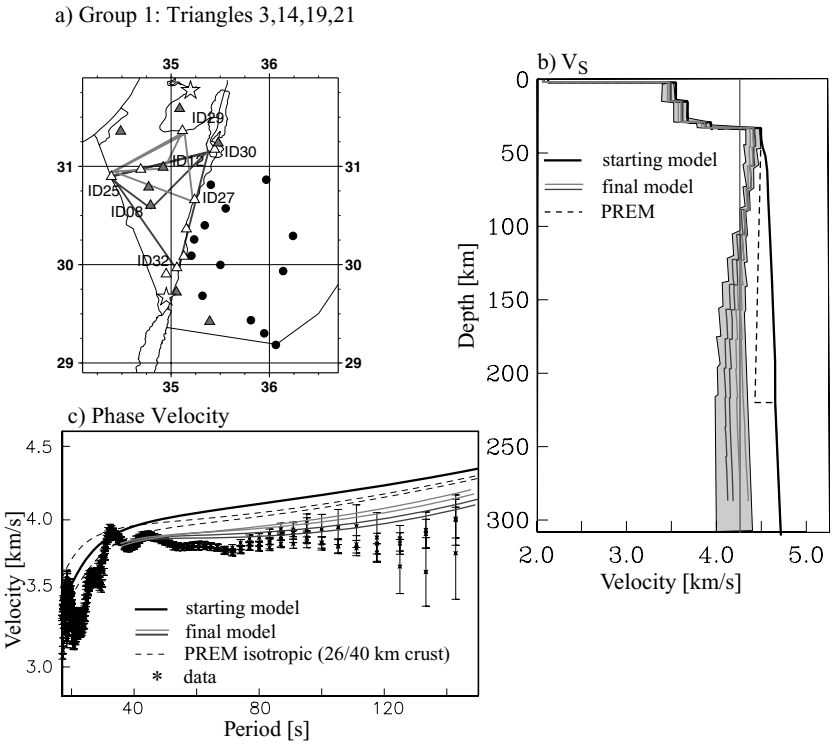

Figure 14. Results from velocity modelling for the four station triangles 3, 14, 19 and 21 (group 1). (a) Location of the triangles; Sensor types are coded as in Fig. 1). (b) Velocity models resulting from the inversions (dark, medium grey) and corridor of possible models for an acceptable range along the trade-off curve resulting from minimizing eq. (2) (light grey area). Also shown are the starting model (solid black) and isotropic PREM for the mantle (dashed; for clarity, the crustal part is omitted). The vertical grey line marks $V_S = 4.25$ km s^{-1}; (c) phase velocity measurements (symbols) and model predictions (dark, medium grey). The two dashed lines mark predictions for PREM with a modified 26- and 40-km-thick crust. The grey shades in the model and prediction correspond to the grey shades of the four triangles.

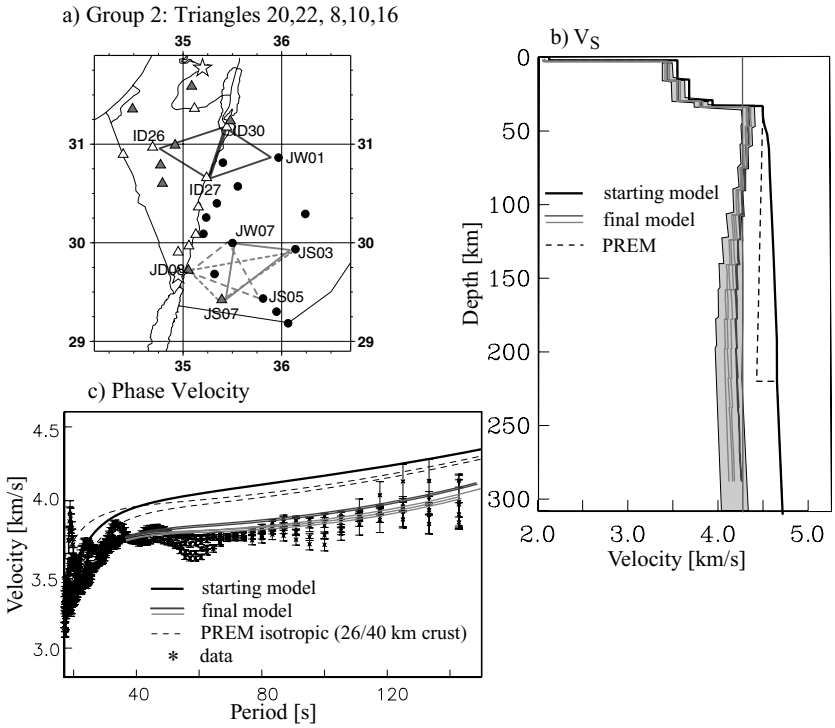

Figure 15. Results from velocity modelling for the four station triangles 20, 22 to the north and 8, 10, 16 to the south of the Arava/Araba Fault (group 2). For details see Fig. 14. For clarity, different dash lengths are used for the triangles in a).

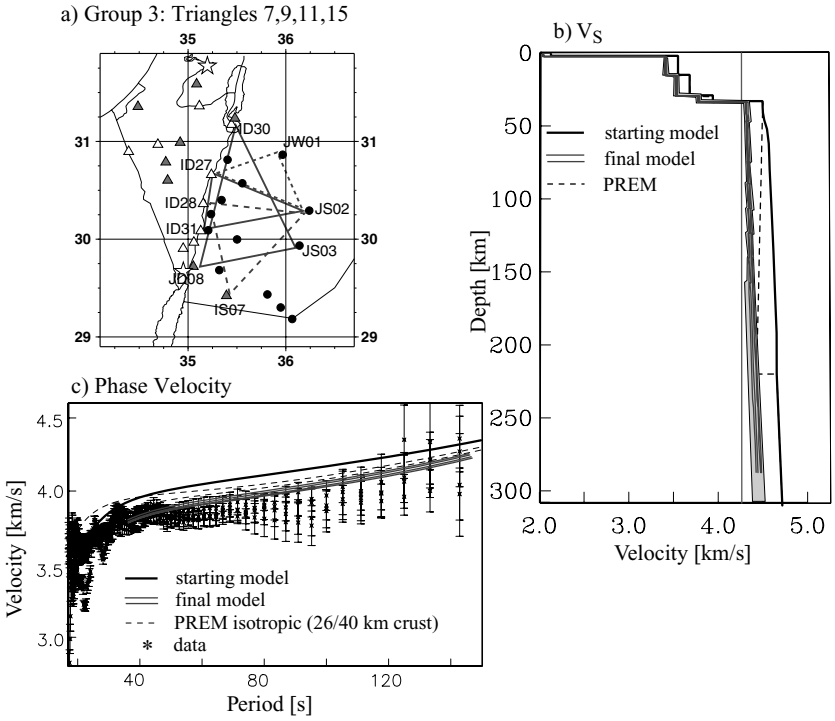

Figure 16. Results from velocity modelling for the four station triangles 7, 9, 11 and 15 (group 3). For details see Fig. 14.

significantly lower velocities in the lithosphere. Indeed, we observe a similar trend in shear velocity with depth as for Group 1 triangles but the velocities in the lithosphere are only around 4.31 km s^{-1} and are 2.7 per cent lower than for Group 1 triangles. We can identify two areas for which we observe this trend. One area is near the southern end of the DESERT array where the mantle may be affected by rifting effects of the Red Sea. The other area is in the north near the Dead Sea Basin, on both sides of the DST. Velocities in the asthenosphere are essentially the same as those found for Group 1. The velocity contrast in the lithosphere is well resolved as phase data at periods between 40 and 85 s best constrain the lithosphere (Fig. 13). This is the period range for which we can measure dispersion with the highest precision.

A third group of triangles to the east of the DST (Group 3), away from the northern and southern boundaries of the array, gives somewhat intriguing results. Fig. 16(c) indicates that phase velocities scatter more than in the other two groups but generally increase with period and approach predictions for PREM. This implies that the deep structure must be close to that of PREM, while shallow structure is expected to be slower than PREM. The results from formal inversions confirm this as shown in panel b. The lithosphere has velocities that we find for other triangles east of the DST but the asthenosphere exhibits higher velocities that reach those of PREM at depths around 200 km. Below that, our data set cannot resolve structure. For this group of triangles, we do not observe a decrease of shear velocity with depth as we see for the other triangles. It is arguable that the involvement of CMG-40T sensors in these triangles may not allow us to determine structure in the asthenosphere. This issue is discussed further in the next section.

We should note that the final models do not depend greatly on the starting model as long as the latter stays realistic and lies within the limits shown here. We test this with triangles 14 (group 1) and 15 (group 3). A starting model that is 4.5 per cent slower above 300 km than the one we used here yields models that are about 1 per cent slower above 80 km than the ones we get with the faster starting model, for both triangles. The change diminishes with depth. In this test, we keep the regularization parameter fixed. The change in models is within the error bars given by the trade-off curve. We do not find a compelling reason why we should choose different starting models for the mantle and different regularization parameters west and east of the DST.

Our final step is to combine the results of all triangles into one 3-D model which is shown in Fig. 17. We define a 0.05° grid and average the results of all triangles that involve each gridpoint. Most likely, this process results in an over-smoothed model of real structure. On the other hand, the wavelengths of the surface waves considered here are longer than most of the triangles used here, so this step may be justified. As indicated above, we find a marked difference in shear velocity west and east of the DST. This difference is most pronounced in the shallow lithosphere and decreases with depth. At 110 km, this difference is no longer discernible. Below that, velocities in the asthenosphere decrease west of the DST and east near the northern and southern boundaries of the array. At these depths, a strong high velocity anomaly can be found east of the DST, away from the array boundaries. This anomaly appears to become stronger towards the east. To estimate the robustness of the model, we determined errors at each gridpoint as the weighted sum of hitcount, the number of triangles covering a point (Fig. 18), and the velocity variance among triangles at this point. Fig. 19 indicates that errors in the lithosphere are slightly larger to the west of the DST than to the east and amount to roughly 0.5 per cent. At shallow depths, increased uncertainties basically reflect a lack of coverage. The hitcount is less relevant at greater depths were errors get larger. They reach 1 per cent near the bottom where velocity estimates to the east of the DST are less certain than to the west, even in well-covered areas.

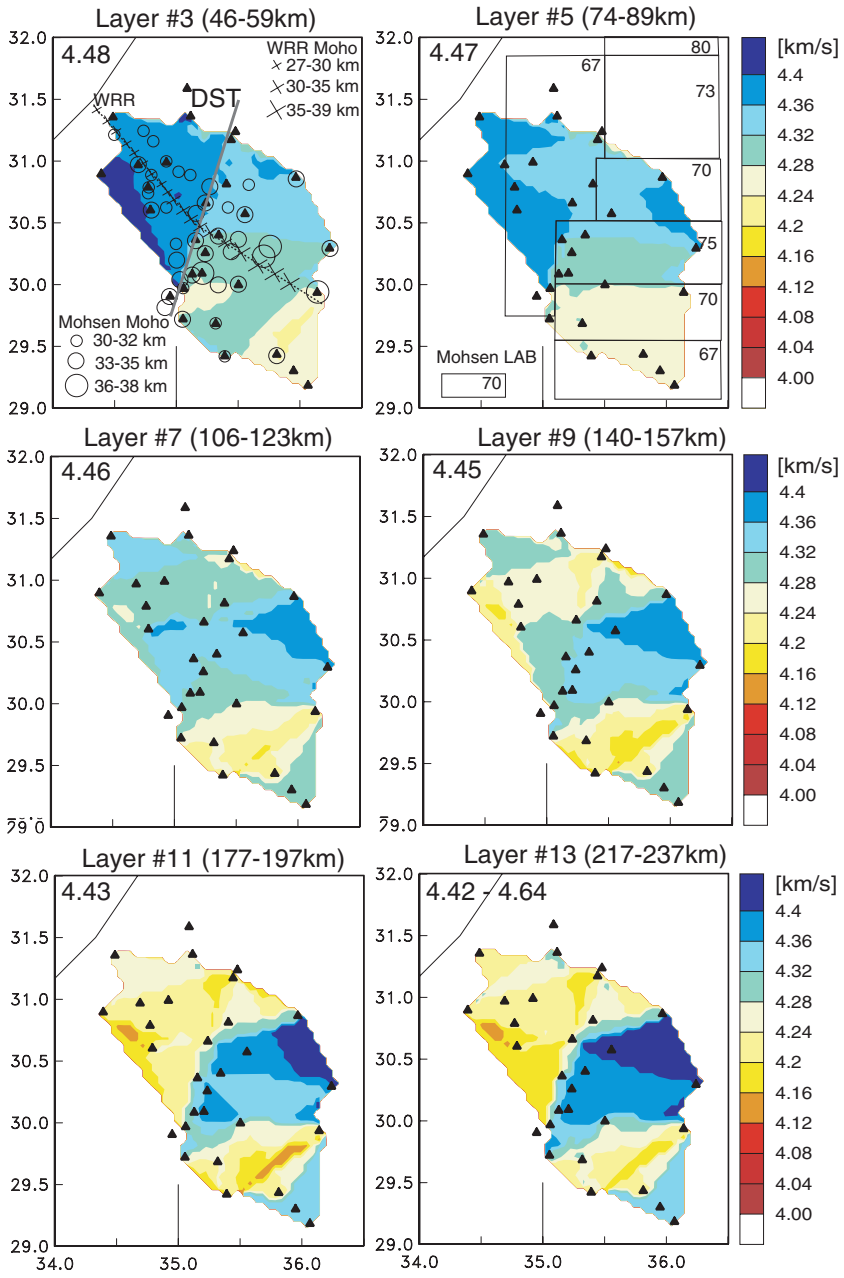

Figure 17. Shear velocity variation in six of the 15 layers in our model. The model is defined on a 0.05° grid and then smoothed. Errors in the model are displayed in Figure 19. A number in the upper Left-hand corner in each panel denotes average velocities in isotropic PREM. The upper two panels summarize the results for Moho and lithosphere-asthenosphere boundary depth from Mohsen *et al.* (2005, 2006) and the Moho depth along the WRR line (DESERT group 2004).

6 DISCUSSION

6.1 Velocity variations in the lithosphere

Along the Arava/Araba Valley, we find a pronounced velocity contrast across the DST in the lithosphere with a velocity jump of the order of 2 per cent. This contrast appears to diminish to the north towards the Dead Sea Basin. The formal errors are no more than 0.5 per cent so the 2 per cent-velocity jump is significant. There exists a small trade-off between crustal thickness and velocities in the lithosphere. In our initial inversions, we had included dispersion data to a frequency of up to 31 mHz ($T = 32$ s), to invert for a 10-layer model. Using the phase velocities of triangle #3 of Group 1 (Fig. 14), our inversions resulted in a less that 2 per cent shear velocity reduction in the lithosphere when we allowed the crustal thickness to decrease from 37 to 26 km. This implies that our velocities could be biased low if we underestimate crustal thickness and high if we overestimate it. To reduce this bias, we included only data up to 28.5 mHz ($T = 35$ s), to invert for a 15-layer model that allows for a finer parametrization. In this case, the bias is no more than 0.5 per cent which is on the order of the formal errors of Fig. 19 and therefore not significant. We choose a fixed crustal thickness of 33 km in our start model so the bias should be less than 0.25 per cent. The final models depend somewhat on the starting

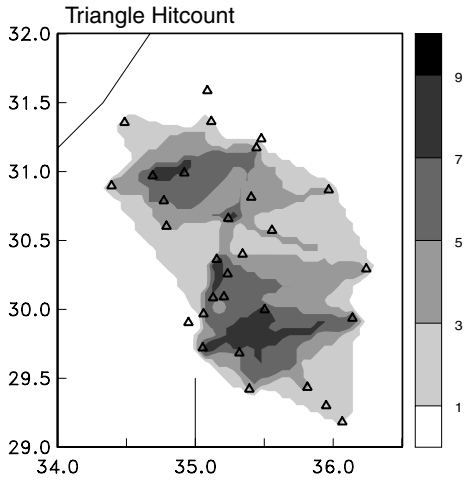

Figure 18. Hitcount for each 0.05° gridpoint in our model. Hit count is defined as the number of triangles that involve a particular gridpoint.

model, and changes can be more than 0.5 per cent. However, trends are the same for models on both sides of the DST and we find no compelling reason to choose different starting models that could potentially diminish the 2 per cent-jump across the DST.

There is no evidence from the wide-angle refraction seismic study that the Moho reaches deeper than 37 km along the WRR profile (DESERT Group 2004) though Moho depths in Jordan appear to be slightly greater than in Israel. In their receiver function study, Mohsen *et al.* (2005) find the crust to be between 32 and 38 km though the latter values are found only at two stations, JS03 and a short-period station along the WRR profile northeast of station JW07. In a body wave tomographic study using ISC data, Koulakov & Sobolev (2006) find Moho depths of around 33 km in the area but crustal thickness could increase to 37 km east of 36° E, which is near the eastern end of the DESERT array (see also Götze *et al.* 2007). Mohsen *et al.* (2005) find that the crust is no less than 31 km thick in the west, while the Moho map of Koulakov & Sobolev (2006) shows a decrease in crustal thickness towards the Mediterranean Sea to values below 26 km though this is confined to coastal areas, north of the DESERT array. Given these studies and our results, there is a chance that some of the velocity gradient we find in the lithosphere across the DST may come from the bias by not accounting for variations in Moho depth but the effects are small and the difference in the lithosphere across the DST appears to be real.

The shallow lower velocities found on the Arabian Peninsula may indicate that the lithosphere there was altered by cenozoic volcanism. If thermal effects are the dominant cause for changes in velocities, and not melt or compositional changes, the velocity contrast scales directly with a contrast in density (eq. 1) which could go a long way to explain the impressive change in topography of about 1 km across the DST. Many of our triangles are aligned with the DST or terminate there. One could argue that such a model parametrization implicitly introduces a boundary in the model that may not exist in the real world but we doubt that this is the case. Sobolev *et al.* (2005) present a thermomechanical model for the dynamics of the Dead Sea Transform to explain a variety of geophysical observables. Starting with a uniform lithosphere, they argue that the inclusion of minor transform-perpendicular extension and lithosphere erosion east of the DST are necessary to cause the local relief observed across the main Arava Fault.

6.2 The bottom of the lithosphere and the asthenosphere

Sobolev *et al.* (2005) argue that a mantle plume intruding from the south may have been the cause for a thinning of the lithosphere east of the DST. Their favoured model 3 has a markedly thicker lithosphere in the west than in the east. An early receiver function analysis at the DESERT array may have suggested this but the final analysis tells a different story. Mohsen *et al.* (2006) argue that the resolution of the lithosphere-asthenosphere boundary (LAB) is relatively poor across the DESERT array. They find the LAB to the west of the DST at about 67 km. In the east, they find a thinning of the lithosphere from about 80 km in the north to 67 km in the south, which provides no evidence for a thinning across the DST from west to east across the Arava Valley, as Sobolev *et al.* (2005) suggest. Perhaps, the geodynamic processes involved have affected the entire study area and one needs to look further east for a 'baseline' lithosphere-asthenosphere system. For example, Mohsen *et al.* (2006) find much thicker lithosphere (160 km) on the stable Arabian Peninsula, well to the southeast of the DESERT array. A comparison with a recent *P*-velocity model by Koulakov *et al.* (2006) is somewhat intriguing. They find high velocities in the lower lithosphere to the west of the DST which is roughly consistent with our model. However, to the east of the DST, they find a trend from low velocities in the north to high velocities in the south which appears inconsistent with both the receiver function study as well as our surface wave study. Setting significantly different depth resolution aside, such a mismatch between velocity anomalies could be indicative of compositional variations or local changes in seismic anisotropy that is ignored in both studies.

At depths greater than 100 km, we find velocities in the asthenosphere that are significantly lower than that of PREM (by roughly 4 per cent). It appears difficult to reconcile such low velocities with realistic thermomechanical models (Stephan Sobolev, 2004, personal communication). On the other hand, anelastic effects can increase temperature derivatives for elastic velocities by a factor of two (Karato 1993) so that smaller changes in temperature would be required to fit observed velocity anomalies. It is conceivable that Sobolev's estimates of attenuating effects are too conservative. Indeed, recent seismic observations suggest that the uppermost mantle in the greater area, extending from the Red Sea north towards Asia Minor, is unusually highly attenuating (Gung & Romanowicz 2004). Sobolev's model also does not explain high temperatures that are inferred from xenoliths found in the Dead Sea area and elsewhere in Jordan (H.J. Förster 2004, R. Oberhänsli, 2004, personal communication). Although the surface heat flow in Jordan revealed that the steady-state Phanerozoic geotherm may be hotter than previously thought, the thermal signal from the relatively young geological processes may not yet have reached the surface to produce a significant heat flow signal (Förster *et al.* 2007). This allows for the possibility that the mantle has been altered enough to produce a seismic signal. Our study is not the only one that finds extremely low seismic velocities in the area. In global surface wave models, the greater Afar Triangle-Red Sea area hosts one of the most pronounced low velocity anomalies in the world (e.g. Ekström *et al.* 1997; Levshin *et al.* 2005). In a semi-regional study covering 2/3 of Africa, the Arabian Peninsula and most of southern Eurasia, Debayle *et al.* (2001) find that velocities in the greater Dead Sea area may be less than 4 km s^{-1} at 100 km depth. This is also supported by the study of Maggi & Priestley (2005) who investigate the Turkish–Iranian plateau.

The thermal thinning hypothesis of Sobolev and his colleagues may explain some of the anomalies we observe in the

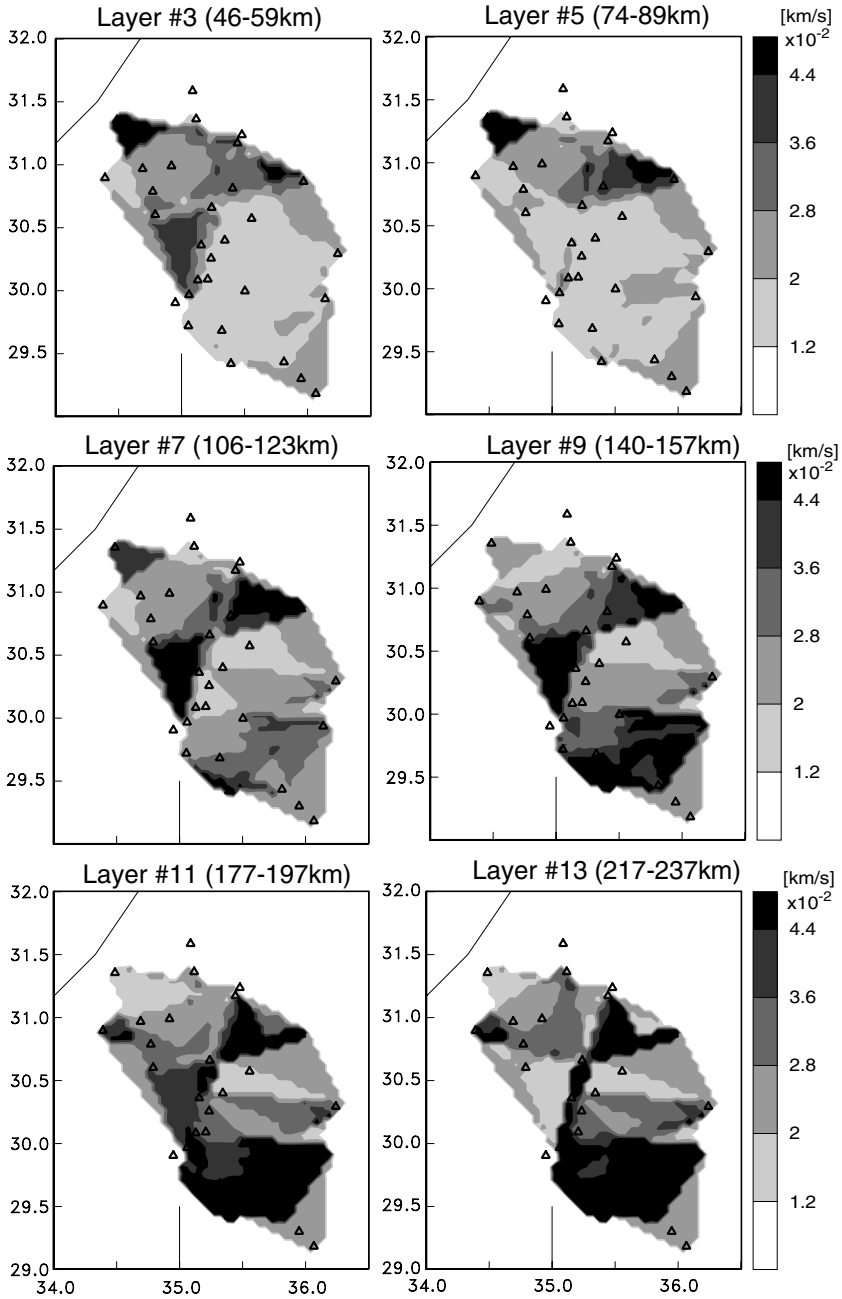

Figure 19. Error maps for the model shown in Fig. 17. Errors are determined as a weighted sum of rms for each gridpoint and the number of triangles a gridpoint was hit by (see Fig. 18). Errors are of the order of less than 1 per cent and are largest at greater depths, east of the DST.

asthenosphere but thermal effects alone appear to be insufficient to cause the low velocities in the region. Rather, a higher melt-content could lower velocities significantly. Ignoring effects from strong azimuthal anisotropy can bias estimates of isotropic velocity anomalies low if earthquakes sample mostly the slow direction of local anisotropy. The data errors and the azimuthal distribution of data is not optimal to observe azimuthal anisotropy but we find no obvious azimuthal dependencies. The following considerations speak against a strong bias. The Dead Sea area is dominated by plate motion in the north–northeast to south–southwest direction and only a small amount of extension is proposed across the DST by Sobolev *et al.* (2005). The earthquakes in our study cover azimuths primarily in the northeastern quadrant with many backazimuths being around 45°, which is within 20° of the direction of plate motion. With such data sampling, our estimates may be biases high and are likely not biased low.

Again somewhat intriguing is our disagreement with the *P* velocity model by Koulakov *et al.* (2006) who find high velocities between 120 and 200 km depth west of the DST but relatively low velocities to the east. East of the DST, their gradient from higher velocities in the north to lower velocities in the south at 200 km depth actually reflects our own, which is in contrast to what they observe at shallower depths. We currently have no explanation for this disagreement. We speculate, however, that while their lateral resolution is probably far superior to ours, their vertical resolution likely does not match ours. Koulakov *et al.* (2006) largely observe

negative traveltime anomalies west of the DST, implying seismically fast structure beneath, and positive anomalies to the east. In a hypothesis test we predict vertical *S* traveltime anomalies through our model. Considering that their ray coverage decays with depth, we search for a depth level for which the structure above produces the contrast they observe across the DST. We predict indeed negative anomalies west of the DST and positive anomalies to the east when we truncated our mantle model at 150 km or above. This is about the depth range for which Koulakov *et al.* (2006) have the best ray coverage, and ray incidence is nearly vertical. An unresolved outcome of this test is the fact that we predict strong positive anomalies to the extreme southeast where Koulakov *et al.* (2006) find the 'fastest' traveltimes. It is noteworthy that Koulakov & Sobolev (2006) also find vastly different structure in *S* and *P*-velocity across the DST, just above and below the Moho. Such a disagreement could be indicative for a complex set of mechanisms that are responsible for the seismic anomalies including differences in melt fraction and variations in attenuation, anisotropy and petrology.

6.3 Apparent heterogeneity induced by the instrumentation

Given the fact that our study is not set up to constrain boundaries, such as the LAB, but only velocity variations with depth, the results of Mohsen *et al.* (2006) are consistent with what we find, the only exception being the high-velocity anomaly in the asthenosphere towards the northeastern end of the DESERT array. Though these velocities are physically not implausible—recall the velocities approach those of PREM—we fall short of finding a convincing explanation for this heterogeneity in the asthenosphere unless we actually see the effects of a nearly unaltered Arabian Shield away from the DST. There is a remote possibility that Mohsen *et al.* (2006) do not detect this piece of lithosphere in their study due to the sparse station distribution in northeastern Jordan. It is also worth pointing out that in receiver function studies, the depth to discontinuities trades-off with the velocities above them. If Mohsen *et al.* (2006) let the velocities in the lithosphere vary across the DESERT array, our results may actually converge.

On the other hand, two factors make the deep high velocity anomaly in the northeast uncertain in our study. Fig. 18 shows that areas to the northwest and south are well covered. Structure in the northeast is constrained by only one or two triangles, which increases relative uncertainties in the model. Perhaps more importantly, virtually all of the triangles in the east involve records of CMG-40T sensors whose bandwidth is severely limited compared to true broad-band sensors. Though numerical results indicate that structure at 150 km or even deeper should be resolved, it is possible that our error analysis does not account fully for the deficiency in sensor quality. The analysis of a follow-up deployment of 6 CMG-3Ts in Jordan is currently ongoing and will hopefully shed light on these unresolved issues.

ACKNOWLEDGMENTS

We wish to thank editor Jeannot Trampert, two anonymous reviewers, Andrea Förster and Stephan Sobolev for helpful comments that helped improve this manuscript. The experiment was funded by the Deutsche Forschungsgemeinschaft (German Research Foundation), the GeoForschungsZentrum (GFZ) and the German Minerva Foundation. The research presented here was funded by U.S. National Science Foundation grant OCE-95-29707 and EAR-03-36864. The stations were provided by the Geophysical Instrument Pool Potsdam at GFZ and the data are archived at the GEOFON data management center. Some maps were drawn using the generic mapping tool (GMT) (Wessel & Smith 1998).

REFERENCES

Abu-Ayyash, K. & the DESERT Team, 2000. Multinational Geoscientific Research Effort Kicks Off in the Middle East, *EOS, Trans. Am. geophys. Un.,* **81,** 609–617.

Aldersons, F., Ben-Avraham, Z., Hofstetter, A., Kissling, E. & Al-Yazjeen, T., 2003. Lower-crustal strength under the Dead Sea basin from local earthquake data and rheological modelling. *Earth planet. Sci. Lett.,* **214,** 129–142.

Alsina, D. & Snieder, R., 1993. A test of the great circle approximation in the analysis of surface waves, *Geophys. Res. Let.,* **20,** 915–918.

Amiran, D.H.K., Arieh, A. & Turcotte, T., 1994. Earthquakes in Israel and adjacent areas: macroseismicity observations since 100 B.C.E., *Israel Explor. J.,* **41,** 261–305.

Anderson, O.L. & Isaak, M., 1995. Elastic constants of mantle minerals at high temperature, in *Mineral Physics and Crystallography, AGU Ref. Shelf # 2*, pp. 64–97, ed. Ahrens, T.J., Washington, DC.

Anderson, O.L., Schreiber, E., Liebermann, R.C. & Soga, M., 1968. Some elastic constant data on minerals relevant to geophysics, *Rev. Geophys.,* **6,** 491–524.

Backus, G. & Gilbert, F., 1968. The Resolving Power of Gross Earth Data, *Geophys. J. R. astr. Soc.,* **16,** 169–205.

Bassin, C., Laske, G. & Masters, G., 2000. The current limits of resolution for surface wave tomography in North America, *EOS, Trans. Am. geophys. Un.,* **81,** F897.

Ben-Avraham, Z., Hänel, R. & Villiger, H., 1978. Heat flow through the Dead Sea Rift, *Mar. Geol.,* **28,** 253–269.

Bock, G., Hofstetter, R., Mohsen, A. & Rümpker, G., 2001. Evidence for olivine alignment parallel to the Dead Sea Transform from shear wave splitting analysis, *EOS, Trans. Am. geophys. Un.,* **82,** F825.

Debayle, E., Leveque, J.-J. & Cara, M., 2001. Seismic ev idence for a deeply rooted low-velocity anomaly in the upper mantle beneath the northeastern Afro/Arabian continent, *Earth planet. Sci. Let.,* **193,** 423–436.

DESERT Group, 2004. The crustal structure of the Dead Sea Transform, *Geophys. J. Int.,* **156,** 655–681.

Dziewonski, A.M. & Anderson, D.L., 1981. Preliminary reference Earth model, *Phys. Earth planet. Inter.,* **25,** 297–356.

Eckstein, G., 1979. Review of Heat Flow Data from the Eastern Mediterranean Region, *Pageoph.,* **117,** 150–159.

Ekström, G., Tromp, J. & Larson, E., 1997. Measurements and global models of surface wave propagation, *J. geophys. Res.,* **102,** 8137–8157.

Forsyth, D.W., Webb, S.C., Dorman, L.M. & Shen, Y., 1998. Phase velocities of Rayleigh waves in the MELT experiment on the East Pacific Rise, *Science,* **280,** 1235–1238.

Förster, A., Förster, H.-J., Masarweh, R., Masri, A., Tarawneh, K. & DESERT Group, 2007. The surface heat flow of the Arabian Shield in Jordan, *J. Asian Earth Sci.,* **30,** 271–284, doi:10.1016/j.jseaes.2006.09.002.

Friederich, W., Wielandt, E. & Stange, S., 1994. Non-plane geometries of seismic surface wavefields and their implications for regional surface-wave tomography, *Geophys. J. Int.,* **119,** 931–948.

Galanis, S.P., Sass, J.H., Munroe, R.J. & Abu-Ajamieh, M., 1986. Heat flow at Zerqa Ma'in and Zara and a geothermal reconnaissance of Jordan, *US Geological Survaey, Open File Report 86–63, Menlo Park*.

Garfunkel, Z. & Ben-Avraham, Z., 1996. The structure of the Dead–Sea basin, *Tectonophys.,* **266,** 155–176.

Gilbert, F. & Dziewonski, A.M., 1975. An application of normal mode theory to the retrieval of structural parameters and source mechanisms from seismic spectra, *Phil. Trans. R. Soc. Lond., A,* **278,** 187–269.

Götze, H.-J., El-Kelani, R., Schmidt, S., Rybakov, M., Förster, H.J., Ebbing, J. & the DESERT Group, 2007. Integrated 3-D density modelling and segmentation of the Dead Sea Transform, *Int. J. Earth Sci.,* **96**. 289–302, doi:10.1007/s00531-006-0095-5.

Gung, Y. & Romanowicz, B., 2004. *Q* tomography of the upper mantle using three-comonent long-period waveforms, *Geophys. J. Int.,* **157,** 813–830.

Haberland, C. et al., 2003. Modeling of seismic guided waves at the Dead Sea Transform, *J. geophys. Res.,* **108,** 2342, doi:10.1029/2002JB002309.

Hofstetter, A., Thio, H.K. & Shamir, G., 2003. Source mechanism of the 22/11/1995 Gulf of Aqaba earthquake and its aftershock sequence, *J. Seismol.,* **7,** 99–114.

Karato, S., 1993. Importance of anelasticity in the interpretation of seismic tomography, *Geophys. Res. Lett.,* **20,** 1623–1626.

Kesten, D., Weber, M., Haberland, C., Janssen, C., Agnon, A., Bartov, Y., Rabba, I. & the DESERT Group, 2008. Combining satellite and seismic inages to analyse the shallow structure of the Dead Sea Transform near the DESERT transect, *Int. J. Earth Sci.*, **97,** 153–169, doi:10.1007/s00531-006-0168-5.

Klinger, Y., Avouac, J., Karaki, N.A., Dorbath, L., Bourles, D. & Reyss, J.L., 2000a, Slip rate on the Dead Sea transform fault in northern Araba valley (Jordan), *Geophys. J. Int.,* **142,** 755–768.

Klinger, Y., Avouac, J., Dorbath, L., Karaki, N.A. & Tisnerat, N., 2000b. Seismic behavior of the Dead Sea fault along Araba valley, Jordan. *Geophys. J. Int.,* **142,** 769–782.

Koulakov, I. & Sobolev, S.V., 2006. Moho depth and three-dimensional *P* and *S* structure of the crust and uppermost mantle in the Eastern Mediterranean and Middle East derived from tomographic inversion of local ISC data, *Geophys. J. Int.,* **164,** 218–235.

Koulakov, I., Sobolev, S.V., Weber, M., Oreshin, S., Wylegalla, K. & Hofstetter, R., 2006. Teleseismic tomography reveals no signature of the Dead Sea Transform in the upper mantle structure, *Earth planet. Sci. Let.,* **252,** 189–200.

Laske, G., 1995. Global observation of off-great-circle propagation of long-period surface waves, *Geophys. J. Int.,* **123,** 245–259.

Laske, G. & Cotte, N., 2000. Surface Wave Propagation Effects at the Saudi Seismic Network, in *SRS 22nd Annual DoD/DoE Seismic Research Symposium, New Orleans*, CD-ROM file number 04-0006.pdf, 10pp.

Laske, G. & Cotte, N., 2001. Surface Wave Waveform Anomalies at the Saudi Seismic Network, *Geophys. Res. Let.,* **28,** 4383–4386.

Laske, G. & Masters, G., 1996. Constraints on global phase velocity maps by long-period polarization data, *J. geophys. Res.,* **101,** 16 059–16 075.

Laske, G., Phipps Morgan, J. & Orcutt, J.A., 1999. First Results from the Hawaiian SWELL Pilot Experiment, *Geophys. Res. Lett.,* **26,** 3397–3400.

Laske, G., Phipps Morgan, J. & Orcutt, J.A., 2007. The Hawaiian SWELL Pilot Experiment – Evidence for Lithosphere Rejuvenation from Ocean Bottom Surface Wave Data, *GSA Special Paper 430,* doi: 10.1130/2007.2430(11).

LeBeon, M, Y. *et al.*, 2006. Geodetic versus geologic slip rate along the Dead Sea Fault. *Seism. Soc. Am. Ann. Meet. San Francisco, USA April, 18–22*.

Levshin, A.L., Barmin, M.P., Ritzwoller, M.H. & Trampert, J., 2005. Minor–arc and major-arc global surface wave diffraction tomography., *Phys. Earth planet. Int.,* **149,** 205–223.

Maggi, A. & Priestley, K., 2005. Surface waveform tomography of the Turkish-Iranian plateau. *Geophys. J. Int.,* **160,** 1068–1080.

Mahmoud, S., Reilinger, R., McClusky, S., Vernant, P. & Tealeb, A., 2005. GPS evidence for northward motion of the Sinai Block: implications for E. Mediterranean tectonics. *Earth Planet. Sci. Lett.,* **238,** 217–224.

Makris, J., Ben-Avraham, Z., Behle, A., Ginzburg, A., Giese, P., Steinmetz, L., Witmarsch, R.B. & Elefheriou, S., 1983. Seismic refraction profiles-between Cyprus and israel and their interpretations, *Geophys. J. R. astr. Soc.,* **75,** 575–591.

Maercklin, N., Haberland, C., Ryberg, T., Weber, M., Bartov, Y. & DESERT Group, 2004. Imaging the Dead Sea Transform with scattered seismic waves, *Geophys. J. Int.,* **158,** 179–186.

Mechie, J. & El-Isa, Z.H., 1988. Upper lithospheric deformations in the Jordan–Dead Sea tramsform regime, *Tectonophysics,* **153,** 153–159.

Mechie, J., Abu-Ayyash, K., Ben-Avraham, Z., El-Kelani, R., Mohsen, A., Rümpker, G., Saul, J. & Weber, M., 2005. Crustal shear velocity structure across the Dead Sea Transform from two-dimensional modelling of DESERT project explosion seismic data, *Geophys. J. Int.,* **160,** 910–924.

Meier, T., Dietrich, K., Stöckhert, B. & Harjes, H.-P., 2004. One-dimensional models of shear wave velocity for the eastern Mediterranean obtained from the inversion of Rayleigh wave phase velocities and tectonic implications, *Geophys. J. Int.,* **156,** 45–58.

Migowski, C., Agnon, A., Bookman, R., Negendank, J.F.W. & Stein, M., 2004. Recurrence pattern of Holocene earthquakes along the Dead Sea transform revealed by varve-counting and radiocarbon dating of lacustine sediments, *Earth planet. Sci. Lett.,* **222,** 301–314.

Mohsen, A., Hofstetter, R., Bock, G., Kind, R., Weber, M., Wylegalla, K., Rümpker, G. & the DESERT Group, 2005. A receiver function study across the Dead Sea Transform, *Geophys. J. Int.,* **160,** 948–960.

Mohsen, A., Kind, R., Sobolev, S.V., Weber, M. & the DESERT Group, 2006. Thickness of the lithosphere east of the Dead Sea Transform, *Geophys. J. Int.,* **167,** 845–852.

Nur, A. & MacAskill, C., 1991. Earthquakes in the Holy Land; a historical, archaeological and biblical odyssey, *Terra Abstracts,* **3,** 172.

Park, J., Lindberg, C.R. & Vernon, F.L. III, 1987. Multitaper spectral analysis of high-frequency seismograms, *J. geophys. Res.,* **92,** 12 675–12 684.

Reilinger, R. et al., 2006. GPS constraints on continental deformation in the Africa-Arabia-Eurasia continental collision zone and implications for the dynamics of plate interaction, *J. geophys. Res.,* **111,** B0541, doi:10.1029/2005JB004051.

Rümpker, G., Ryberg, T., Bock, G. & Desert Seismology Group, 2003. Boundary-layer mantle flow under the Dead Sea transform fault inferred from seismic anisotropy, *Nature,* **425,** 497–501.

Ryberg, T., Rümpker, G., Haberland, C., Stromeyer, D. & Weber, M., 2005. Simultaneous inversion of shear wave splitting observations from seismic arrays, *J. geophys. Res.,* **110,** B03301, doi:10.1029/2004JB003303.

Salamon, A., Hofstetter, A., Garfunkel, Z. & Ron, H., 2003. Seismotectonics of the Sinai sub-plate he Eastern Mediterranean region. *Geophys. J. Int.,* **155,** 149–173.

Sobolev, S.V., Petrunin, A., Garfunkel, Z., Babeyko, A.Y. & DESERT Group, 2005. Thermo-mechanical model of the Dead Sea Transform, *Earth planet. Sci. Lett.,* **238,** 78–95.

Stange, S. & Friederich, W., 1993. Surface wave dispersion and upper mantle structure beneath southern Germany from joint inversion of network recorded teleseismic events, *Geophys. Res. Lett.,* **20,** 2375–2378.

van Eck, T. & Hofstetter, A., 1990. Fault geometry and spatial clustering of micro-earthquakes along the Dead Sea–Jordan rift fault zone, *Tectonophysics,* **180,** 15–27.

Wdowinski, S. *et al.*, 2004. GPS measurements of current crustal movements along the Dead Sea Fault, *J. geophys. Res.,* **109,** B05403, doi:10.1029/2003JB002640.

Wessel, P. & Smith, W., 1998. New improved version of the Generic Mapping Tools released, *EOS, Trans. Am. geophys. Un.,* **79,** 579.

Wielandt, E., 1993. Propagation and structural interpretation of non-plane waves, *Geophys. J. Int.,* **113,** 45–53.

Woodhouse, J.H. & Wong, Y.K., 1986. Amplitude, phase and path anomalies of mantle waves, *Geophys. J. R. astr. Soc.,* **87,** 753–773.

Woods, M.T. & Okal, E.A., 1996. Rayleigh-wave dispersion along the Hawaiian Swell; a test of lithospheric thinning by thermal rejuvenation at a hotspot, *Geophys. J. Int.,* **125,** 325–339.

Yoshizawa, K., Yomogida, K. & Tsuboi, S., 1999. Resolving Power of Surface Wave Polarization Data for Higher-Order Heterogeneities, *Geophys. J. Int.,* **138,** 205–220.

APPENDIX: MISALIGNMENT OF HORIZONTAL SEISMOMETER COMPONENTS

Our initial data quality assessment routinely includes the inspection of all three seismometer components. Prior to a Love wave dispersion analysis, we examine the frequency-dependent particle motion and measure surface wave arrival angles (Laske 1995). The latter give the direction of approach after propagation in heterogeneous variations in phase velocity. In global studies, arrival angles can be used to retrieve these variations (e.g. Woodhouse & Wong 1986; Laske & Masters 1996; Yoshizawa *et al.* 1999). While this is not

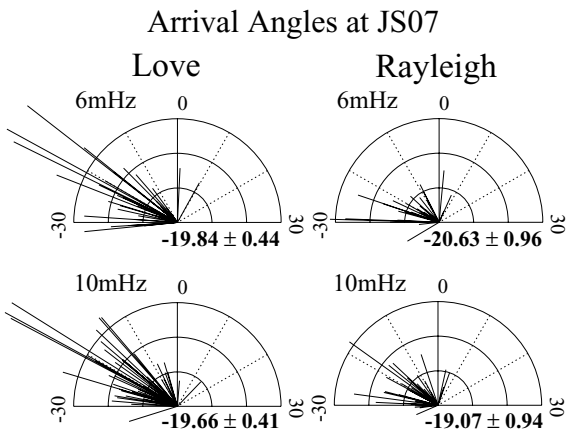

Figure 20. Arrival angles at station JS07, observed for Rayleigh and Love waves at 6 and 10 mHz. The panels show rose diagrams where the polar angle is the arrival angle, the angle away from a source–receiver great circle which is zero for any given earthquake. The length of the vectors represents the reciprocal measurement error. Accurate data with small errors bars tend to stick out of the cluster of observations. A clustering of data in a particular panel could either be due to station misorientation or because the dominance of a certain source–receiver great circle corridor. The numbers below the panels indicate the station misorientations from individual inversions at fixed frequency and wave type.

Table 2. Component misalignment expressed as apparent north.

Station	Apparent North (°)	No. of Rayleigh	No. of Data Love	Sensor	Comment
ID27	4.35 ± 1.60	14	19	STS-2	
ID28	−6.91 ± 0.86	23	29	STS-2	
ID31	−14.01 ± 1.27	17	22	STS-2	
ID32	0.90 ± 0.77	27	26	STS-2	
ID33	0.72 ± 0.98	24	27	STS-2	
ID07	−0.61 ± 0.91	24	34	CMG-3T	(1)
ID08	15.35 ± 0.79	25	33	CMG-3T	
ID10	−4.43 ± 0.85	21	25	CMG-3T	
ID12	−0.04 ± 0.91	19	27	CMG-3T	
JD01	1.31 ± 2.78	4	9	CMG-3T	(2); (3)
JD08	−7.22 ± 0.98	25	33	CMG-3T	1)
JS07	−19.00 ± 0.63	50	56	CMG-3T	
JK02	−3.81 ± 2.53	6	10	CMG-40T	(1); (3)
JS05	−5.48 ± 2.30	8	11	CMG-40T	(3)
JW01	9.63 ± 2.19	11	19	CMG-40T	
JW09	−10.22 ± 2.25	9	14	CMG-40T	(3)

Notes: Apparent north is the angle at which true North appears with respect to the N component of an instrument. Negative values imply a clockwise rotation of the equipment.
(1) N noisy
(2) Noisy most of the time
(3) Uncertain; few data.

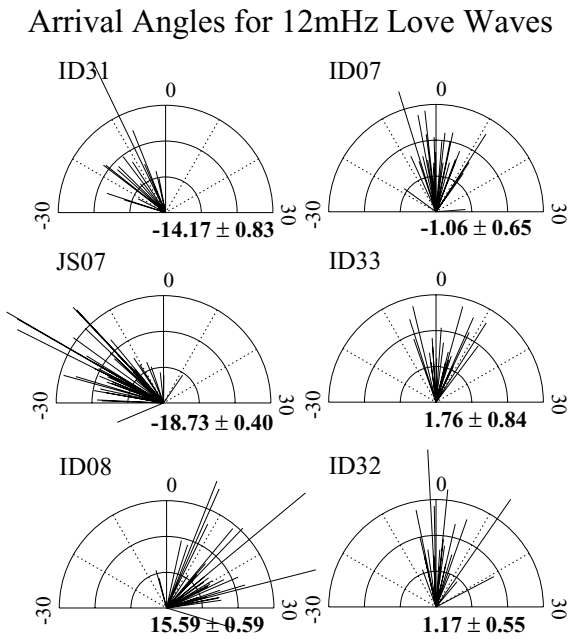

Figure 21. Arrival angles at six stations of the DESERT array, for Love waves at 12 mHz. For details see Fig. 20. Since effects from lateral short-wavelength structure become more dominant with increasing frequency the misorientations for these examples are not included in the final determination of apparent north. Nevertheless, the larger misorientations are consistent with the final values of Table 2.

immediately relevant for the study shown here, a useful by-product is the determination of the orientation of the horizontal seismometer components. A preposition thereby is that the components are orthogonal. The dependence of measured angles on component misorientation is non-linear and we iterate a joint inversion for component misalignment and long-wavelength heterogeneity several times.

Analysing about 18 months of data from the Saudi Seismic Network, Laske & Cotte (2001) show that this technique can be applied successfully on the limited data sets of temporary networks. An important point here is that the data are embedded in a global data set to allow the removal of biases caused by the uneven azimuthal distribution of earthquakes at a particular station. Using this technique we can measure enough arrival angles at most of the stations of the DESERT array to allow for robust determination of component misorientation. Since effects on arrival angles by lateral heterogeneity is expected to increase with frequency, we restrict analysis here to three relatively low frequencies: 6, 8 and 10 mHz. In this case, we do not expect to have a sufficiently large data set to include all of the stations that had CMG-40T sensors. Fig. 20 shows data for 6 and 10 mHz gathered at station JS07. Different wave propagation effects at different frequencies and wave types cause some variation between the four panels but the consistent clustering around about -20° is a strong indication that this station has a significant misorientation. Measuring arrival angles for Love waves is often easier than for Rayleigh waves because the latter are more dispersed and may overlap with the Love wave coda. We therefore typically have Love than Rayleigh wave arrival angles (see Table 2). Fig. 21 shows measurements for 12 mHz Love waves at 6 selected stations. The fact that the arrival angles vary so significantly between stations in a relatively dense network, such as the DESERT array, is also strong indication that some sensors are significantly misoriented.

The joint inversions for long-wavelength heterogeneity and component misalignment often allows us to narrow component misalignment to within less than 1°, as indicated by the numbers in Fig. 21. The weighted average of these numbers over all three frequencies and the two wave types gives the final apparent clockwise rotation of the sensor at JS07 as -19.00 ± 0.63. Table 2 summarizes the final component misorientation for most of the broad-band stations and some of the wide-band stations for which we have enough reliable low-noise data. Several stations are nearly aligned with geographic North but most stations exhibit a moderate misalignment between 0

and 5°. Some stations have a misalignment of more than 5°, where an alignment with geographic North to within 5° appears doable using a compass and a declination map. We obtain a serious misalignment of more than 10° for stations ID31, ID08, JS07 and JW09. It turns out that many of these stations were not installed using a compass but were aligned using the direction of the main road in the area. While a dispersion study is not affected by this misalignment studies using arrival angles to determine phase velocity heterogeneity clearly need to take this into account as do shear wave splitting studies.